5th US Combustion Meeting
Organized by the Western States Section of the Combustion Institute
and Hosted by the University of California at San Diego
March 25-28, 2007.

Scalar filtered mass density functions in non-premixed turbulent jet flames

Tomasz G. Drozda, Guanghua Wang, Vaidyanathan Sankaran, Joseph C. Oefelein, Robert S. Barlow

Combustion Research Facility, Sandia National Laboratories
Livermore, CA 94550, USA

The mixture fraction and temperature filtered mass density functions (FMDF) are studied by analyzing experimental data obtained from one-dimensional (1D) Raman/Rayleigh/LIF measurements of non-premixed $CH_4/H_2/N_2$ turbulent jet flames at Reynolds numbers of 15,200 and 22,800 (DLR-A and B). The experimentally determined FMDFs are conditioned on the Favré filtered values of the mixture fraction and its variance. The filter length scale is normalized by the experimentally determined Batchelor scale. One dimensional filtering, using a top-hat filter, is performed to obtain the FMDFs and the filtered variables used for their conditioning. Emphasis is placed on the shapes of the FMDFs at the fuel- rich, lean and stoichiometric intervals of the filtered mixture fraction. The qualitative shape of the FMDFs is obtained by binning the mass and filter kernel weighted samples. The sensitivity of these shapes to the filter size is also investigated.

1 Introduction

Large eddy simulation (LES) provides an efficient and effective way of studying a broad range of turbulent combustion systems. This effectiveness, however, is only obtained by accurately modeling the subgrid scales (SGS). One SGS modeling approach solves the filtered mass density function (FMDF) transport equation [1–3]. The FMDF describes an instantaneous, mass weighted, distribution of the scalars within the subgrid volume. The LES using the FMDF methods is experiencing a widespread use [4–10] due to its ability to treat reaction source terms in closed form. The mixing of the SGS scalars, however, requires modeling. It is, therefore, of primary interest to investigate the validity of commonly used mixing models. The FMDF is also important in presumed probability density function [11–14] (PDF) or the conditional moment closure [15, 16] methods. Commonly, sets of statistically independent beta PDFs are used in these methods to represent the subgrid joint species distributions.

Previously, Tong *et al.* [17–21] calculated one- and two- dimensional (1D and 2D) filtered density functions (FDF) in non-reacting jets and 1D FDFs and FMDFs in piloted jet flames. They considered conditioning on the filtered mean and SGS variance of the mixture fraction. These two moments were used to study the level of unmixedness of the mixture fraction.

In this work we study the conditional FMDFs of mixture fraction and temperature in non-premixed $CH_4/H_2/N_2$ turbulent jet flames at Reynolds numbers of 15,200 and 22,800 (DLR-A and B). The

FMDFs are conditioned on fuel- lean, stoichiometric or rich values of the Favré filtered mixture fraction and low, medium or high values of the Favré SGS mixture fraction variance. The filter widths are chosen at different locations in the flames as 20 or 40 times the experimentally determined [22] Batchelor scale. We are primarily interested in the shapes of the FMDFs in the context of SGS combustion modeling. In addition, we would like to assess the possibility of using the more easily measurable and more robust temperature data for studying the FMDFs and the process of SGS mixing.

2 Experimental setup and data

The DLR-A and B flames have been used extensively as benchmarks for the TNF Workshop [23, 24]. The jet diameter, d, is 8 mm. The central jet is surrounded by an air coflow. The data considered here has been collected at $x/d = 10,\ r/d = 1.0,\ 1.5$ and $x/d = 20,\ r/d = 1.4,\ 2.0,\ 2.6$, where x and r are the axial and radial directions, respectively.

The experimental setup has been described previously [25–27] and only a brief overview is presented here. Four frequency-doubled Nd:YAG laser beams were combined for the Raman/Rayleigh measurements. The combined beam of roughly 1.6 J/pulse was focused by a 500 mm lens to a waist diameter of about 0.22 mm ($1/e^2$) in the test section. Raman scattered light was collected using a pair of 150 mm diameter achromats (f/2 and f/4). The f/4 lens matched the entrance aperture of an imaging spectrometer, which was fitted with a high-speed rotating mechanical shutter [28]. A back-illuminated, cryogenically cooled CCD camera was used to detect the Raman spectrum. Pixels were binned on chip to form 28 superpixels along the spatial dimension of the CCD, corresponding to a spatial sampling resolution of 0.220 mm along the laser beam, and 14 superpixels along the spectral dimension corresponding to the Raman bands of the major species (CO_2, O_2, CO, N_2, CH_4, H_2O, H_2) and interferences in between. The effective experimental resolution for the combined Raman/Rayleigh/CO-LIF measurements of mixture fraction, including optical blur and data processing effects, is estimated at roughly 0.30 mm.

Rayleigh scattered light was collected by two matched achromats (1:1 imaging). The collected light was focused onto a back-illuminated CCD detector through a 532 nm band-pass filter. Gating was provided by a mechanical leaf shutter. The nominal projected resolution was 0.040 mm, and the optical resolution of the Rayleigh imaging system was approximately 0.050 mm.

The CO LIF imaging system uses the same front collection lens as the Rayleigh system. A dichroic beam splitter in the collimated region reflected CO fluorescence (484 nm) through another matched achromat. An interference filter centered at 484 nm passed the CO fluorescence signal onto an intensified CCD camera. The imaged length for the combined measurements was approximately 6 mm. Typically 6,000 samples were collected at each measurement location.

The mixture fraction was calculated from the measured species mass fractions using Bilger's formulation [29],

$$\xi = \frac{2(Y_C - Y_{C,2})/W_C + (Y_H - Y_{H,2})/2W_H - (Y_O - Y_{O,2})/W_O}{2(Y_{C,1} - Y_{C,2})/W_C + (Y_{H,1} - Y_{H,2})/2W_H - (Y_{O,1} - Y_{O,2})/W_O}, \tag{1}$$

where Y_i's are elemental mass fractions, W_i's are atomic weights, and subscripts 1 and 2 refer to the main jet and coflow air stream, respectively. The stoichiometric value of the mixture fraction

in DLR jet flames is 0.167.

3 Results and discussion

3.1 Properties of the FMDF

Implementation of LES involves the use of the spatial filtering operation,

$$\langle Q(\mathbf{x},t)\rangle_\ell = \int_{-\infty}^{+\infty} Q(\mathbf{x}',t)\mathcal{G}(\mathbf{x}',\mathbf{x})d\mathbf{x}' \tag{2}$$

where $\mathcal{G}$ denotes the filter kernel of width Δ_L, and $\langle Q(\mathbf{x},t)\rangle_\ell$ represents the filtered value of the transport variable $Q(\mathbf{x},t)$. In this work, we consider a top hat filter kernel. In variable density flows it is convenient to consider the Favré filtered quantity, $\langle Q(\mathbf{x},t)\rangle_L = \langle \rho Q\rangle_\ell / \langle \rho\rangle_\ell$.

The "scalar filtered mass density function" (SFMDF, or simply FMDF), denoted by F_ℓ, is formally defined as

$$F_\ell\left(\boldsymbol{\psi};\mathbf{x},t\right) \equiv \int_{-\infty}^{+\infty} \rho\left(\mathbf{x}',t\right)\zeta(\boldsymbol{\psi},\boldsymbol{\phi}(\mathbf{x}',t))\mathcal{G}(\mathbf{x}'-\mathbf{x})\; d\mathbf{x}' \tag{3}$$

$$\zeta(\boldsymbol{\psi},\boldsymbol{\phi}(\mathbf{x},t)) \equiv \delta(\boldsymbol{\psi}-\boldsymbol{\phi}(\mathbf{x},t)) \equiv \prod_{\alpha=1}^{N_s}\delta(\psi_\alpha-\phi_\alpha(\mathbf{x},t)) \tag{4}$$

where δ denotes the Dirac delta function and $\boldsymbol{\psi}$ denotes the sample space of the N_s scalars. The scalar array, $\boldsymbol{\phi}$, may contain the mixture fraction, species mass fractions, enthalpy or temperature. The term ζ is the "fine-grained" density [30, 31], hence Eq. (3) defines the FMDF as the *mass weighted spatially filtered* value of the fine-grained density function. For a fluid density, ρ, equal to unity, Eq. (3) defines a filtered density function (FDF). FMDF and FDF have all of the properties of a PDF [31].

The filtered value of any function of scalar variables, $\hat{Q}$, is obtained by integration over the scalar sample space.

$$\langle\rho\left(\mathbf{x},t\right)\rangle_\ell \langle Q(\mathbf{x},t)\rangle_L = \int_{-\infty}^{+\infty}\hat{Q}(\boldsymbol{\psi})F_\ell(\boldsymbol{\psi};\mathbf{x},t)\; d\boldsymbol{\psi} \tag{5}$$

In particular, the Favré filtered mean and the SGS variance are formally obtained by

$$\langle\rho\left(\mathbf{x},t\right)\rangle_\ell \langle Q(\mathbf{x},t)\rangle_L = \int_{-\infty}^{+\infty}\hat{Q}(\boldsymbol{\psi})\; F_\ell(\boldsymbol{\psi};\mathbf{x},t)\; d\boldsymbol{\psi} = \int_{-\infty}^{+\infty}\rho(\mathbf{x}',t)\; Q(\mathbf{x}',t)\; \mathcal{G}(\mathbf{x}'-\mathbf{x})d\mathbf{x}' \tag{6}$$

and

$$\langle\rho\left(\mathbf{x},t\right)\rangle_\ell \left\langle Q''^2(\mathbf{x},t)\right\rangle_L = \int_{-\infty}^{+\infty}\left(\hat{Q}(\boldsymbol{\psi})-\langle Q\rangle_L\right)^2\; F_\ell(\boldsymbol{\psi};\mathbf{x},t)\; d\boldsymbol{\psi} = \int_{-\infty}^{+\infty}\rho(\mathbf{x}',t)\; \left(Q(\mathbf{x}',t)-\langle Q\rangle_L\right)^2\; \mathcal{G}(\mathbf{x}'-\mathbf{x})d\mathbf{x}' = \left\langle\rho Q^2\right\rangle_\ell / \langle\rho\rangle_\ell - \langle Q\rangle_L^2 \tag{7}$$

3.2 Constructing the FMDF from data

The challenge in obtaining FMDFs from experimental data is illustrated by examining Eq. (3). The FMDF requires a knowledge of the fluid density and the scalar fields, ϕ, as a function of space and time. Three-dimensional fields are needed around a single spatial location where the FMDF is computed. Furthermore, these fields must contain a statistically significant number of samples to accurately predict the moments of interest of the FMDF. In the experiments, the sample significance is usually assured by invoking the Taylor's hypothesis, which allows all temporally uncorrelated instantaneous data to be included as part of the same ensemble. This approach, however, estimates a filtered mass PDF (FMPDF) [32]. That is, including of all instantaneous measurement realizations, collected at a particular location in the flame, in the calculation of the FMDF results in a calculation of a FMPDF.

The process of constructing the single scalar FDF from a one dimensional data is illustrated in Fig. 1 for a unity density case. A qualitative shape of the FDF is constructed by binning of scalar

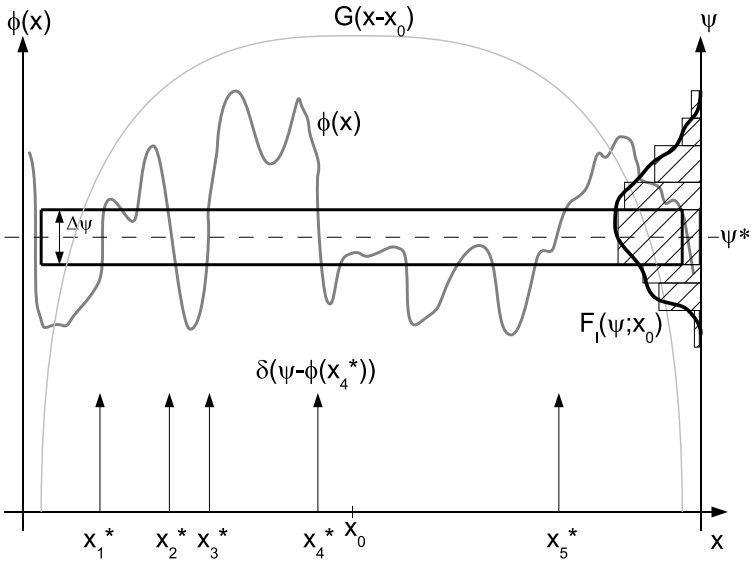

Figure 1: Constructing the one-dimensional FDF. Shown are the scalar variable as a function of space, the filter kernel, $G(x - x_0)$, the fine grained density function, δ, and the FDF for a fixed location of x_0.

data. Figure 1 shows a single bin of width $\Delta\psi$, which horizontally spans the width of the filter kernel. The bin is vertically centered around a scalar sample variable value of ψ^*. The discrete scalar data that fall within this bin are assigned a weight equal to the value of the filter kernel. The sample weights are summed in each bin. For FMDF, the weights equal to the product of the values of the fluid density and the filter kernel. The value for the FDF is obtained by normalizing summed weights by the corresponding bin width and total number of samples in all bins. A histogram, on the vertical right axis, shows the qualitative shape of the FDF. The thicknesses of adjacent columns indicate the respective bin widths. In the current work, the bin widths are determined by ensuring that no less than 80 data points occupy each sample bin. The histogram is constructed by plotting the value for the FMDF at the center of each bin.

The statistical confidence of the constructed FMDFs is assessed using the Monte Carlo Bootstrap Method [33–35]. The results are presented using the error bars that mark the 68.3% confidence intervals. These bars represent the combined effect of statistical errors in the experimental data and physical variability among the uncorrelated instantaneous measurements used in calculating the FMDF..

3.3 Conditional FMDF

The use of all uncorrelated instantaneous measurement realizations in calculating the FMDF provides an estimate of the FMPDF [32]. A qualitative estimate for the FMDF can be constructed by conditioning the FMPDF on a set of functions of the instantaneously measured data. These functions are determined using physical insight relevant to the flame. The conditioned FMPDFs provide a qualitative illustration of the properties of the FMDFs under specific values of interest for the conditioning functions. In previous studies [17–20] the FMPDFs were conditioned on the Favré filtered mean, $\langle \xi \rangle_L$, and its SGS variance, $\langle \xi''^2 \rangle_L$. These two moments were used to study the level of unmixedness of the mixture fraction in piloted diffusion flames. In this work we also condition the FMPDFs on the $\langle \xi \rangle_L$ and $\langle \xi''^2 \rangle_L$, as defined in Eqs. (6,7). For brevity we will refer to these quantities as the mean and the SGS variance. The filtered moments are important conditioning functions because they are typically used as parameters to the SGS combustion models.

Filtering of the experimental data is performed using a filter width that is a multiple of the experimentally determined Batchelor scale, λ_B [22]. The ratio Δ_L/λ_B is set equal to 20 or 40 in the present work. A detailed discussion of the filter size effects is presented in section 3.4.

Figure 2 illustrates the process of constructing the FMDFs from experimental data for the DLR-A flame at $x/d = 20$ and $r/d = 1.4$. Conditioning on both the mean and SGS variance reveals the broad range of FMDFs composing the FMPDF at this particular location. While the FMPDF has a broad asymmetric bimodal shape, the FMDF conditioned only on the fuel-rich interval of the mean exhibits a much narrower, approximately Gaussian, distribution. Double-conditioning the FMDF on high values of the SGS variance reveals a strongly bimodal distribution. Such bimodal distributions quantify the existence of unmixed pockets of scalars within the subgrid. Each marker in Fig. 2a represents a value of the conditioning function computed from a single instantaneous line measurement. To ensure statistical significance for FMDF results, the Taylor hypothesis is invoked and similar values for conditioning functions (i.e. the mean and SGS variance) are binned. The mean bin widths are 0.05 and isolate approximately 900 out of 6000 instantaneous line measurements. The variance bins are found by equipartitioning these measurements data into 5 bins. The high valued bin, for example, contains the line measurements with the top 20% of values for the SGS variance. Such selected bins ensure that the magnitude of the statistical errors associated with FMDFs remains fixed. The medium valued SGS variance bins represent conditioning on a median value of the SGS variance. The distributions of the SGS variances are approximately lognormal.

The widths of the bins are represented visually in Fig. 3. The three sets of 8 vertical lines represent the fuel- lean, stoichiometric and rich conditions in the two flames. Each close pair of vertical lines represents, from left-to-right, the DLR-A and B flames. The set of four close pairs contains information about the downstream location and the ratio of filter width to the Batchelor scale.

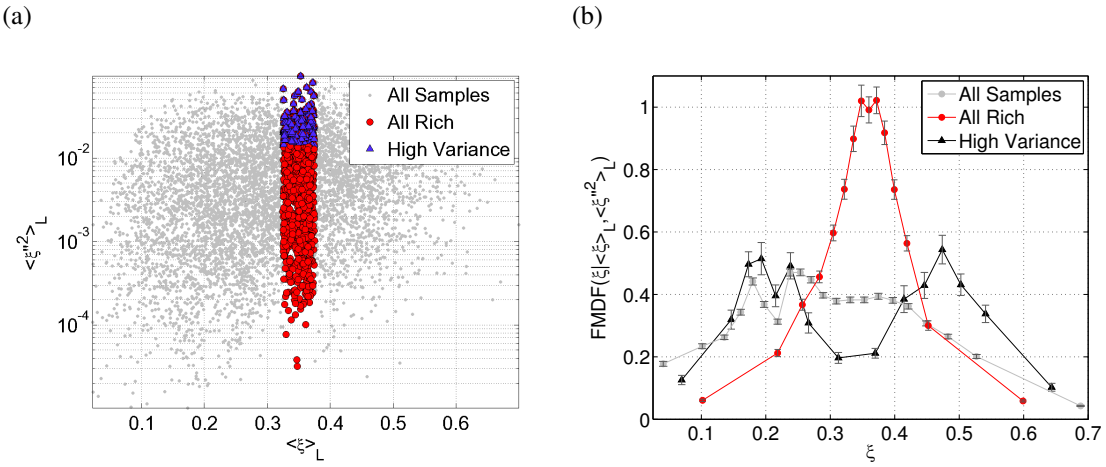

Figure 2: Illustration of a process of constructing the one-dimensional FMDF by conditioning. (a) Favré filtered SGS variance versus the Favré filtered mixture fraction for all available instantaneous measurements at $x/d = 20$, $r/d = 1.4$ and computed with a $\Delta_L/\lambda_B = 40$ (DLR-A). (b) The FMDFs computed from instantaneous measurement realizations found in corresponding bins from (a).

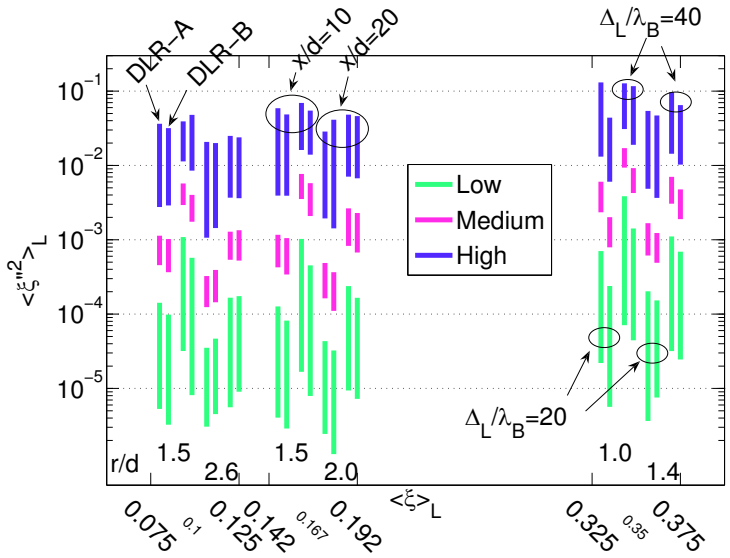

Figure 3: Bin widths used in the calculations of FDFs and FMDFs in the DLR flames.

The difference between the FDF and FMDF is illustrated in Fig. 4. Changes in the magnitude of bimodal peaks, when the FMDFs are conditioned on high values of the SGS variance, are attributed to large differences in the values of the density on the fuel-lean and the fuel-rich sides of the flame. Negative deviations in the density from a value of one depress the FMDF shape with respect to the FDF. In contrast, values greater than unity accentuate the FMDF shape. FDFs and FMDFs represent volumetric and mass distributions of scalars within the subgrid, respectively.

Figure 5 compares the FMDF distributions conditioned on the fuel- rich, stoichiometric, and lean

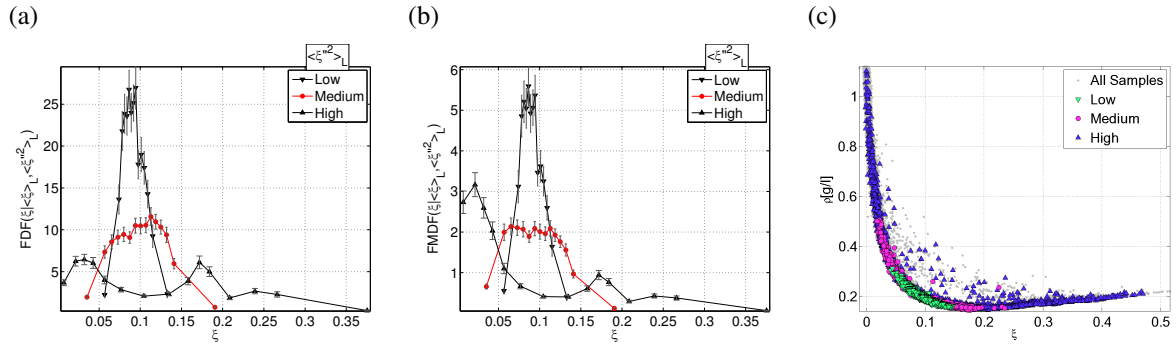

Figure 4: (a) FDF and (b) FMDF conditioned on a lean value of $\langle\xi\rangle_L$ and low, medium and high values of $\langle\xi''^2\rangle_L$ at $x/d = 20$, $r/d = 2.6$ and $\Delta_L/\lambda_B = 40$ (DLR-A). (c) ρ versus ξ of the data used to calculate FDFs and FMDFs in (a) and (b).

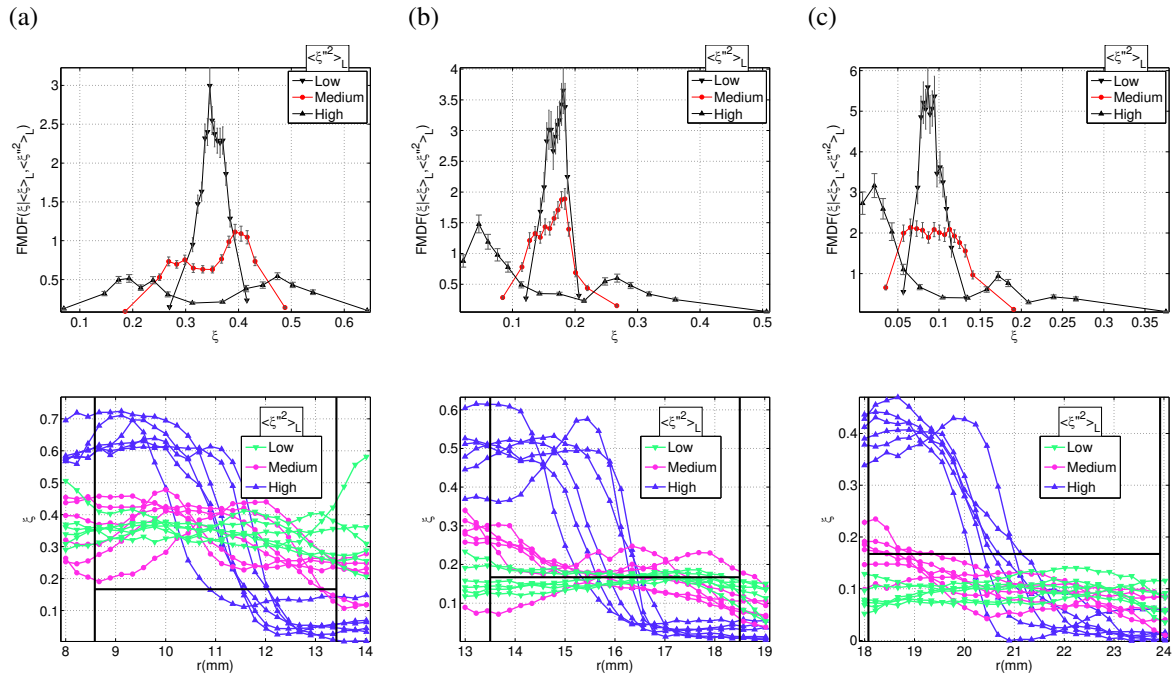

Figure 5: The FMDF conditioning bins, FMDFs of the ξ, and the corresponding representative spatial ξ structures for fuel- (a) rich, (b) stoichiometric, (c) lean values of $\langle\xi\rangle_L$ and low, medium and high values of $\langle\xi''^2\rangle_L$ at $x/d = 20$ and for $\Delta_L/\lambda_B = 40$ for DLR-A.

values of the mean with low, medium and high values of the SGS variance in the DLR-A flame. Several representative spatial profiles are also shown. The two black vertical lines denote the filter width. Only the data enclosed by these lines are used to construct FMDFs. The vertical black line denotes the stoichiometric value of the mixture fraction. Bimodal FMDFs for high valued SGS variance correspond to the spatial "cliff" in mixture fraction. As the mean bin is moved from the fuel- lean to rich side of the flame the peaks of the bimodal FMDFs shift towards the fuel-rich values of the mixture fraction and become equal in magnitude. This indicates a shift in the unmixed

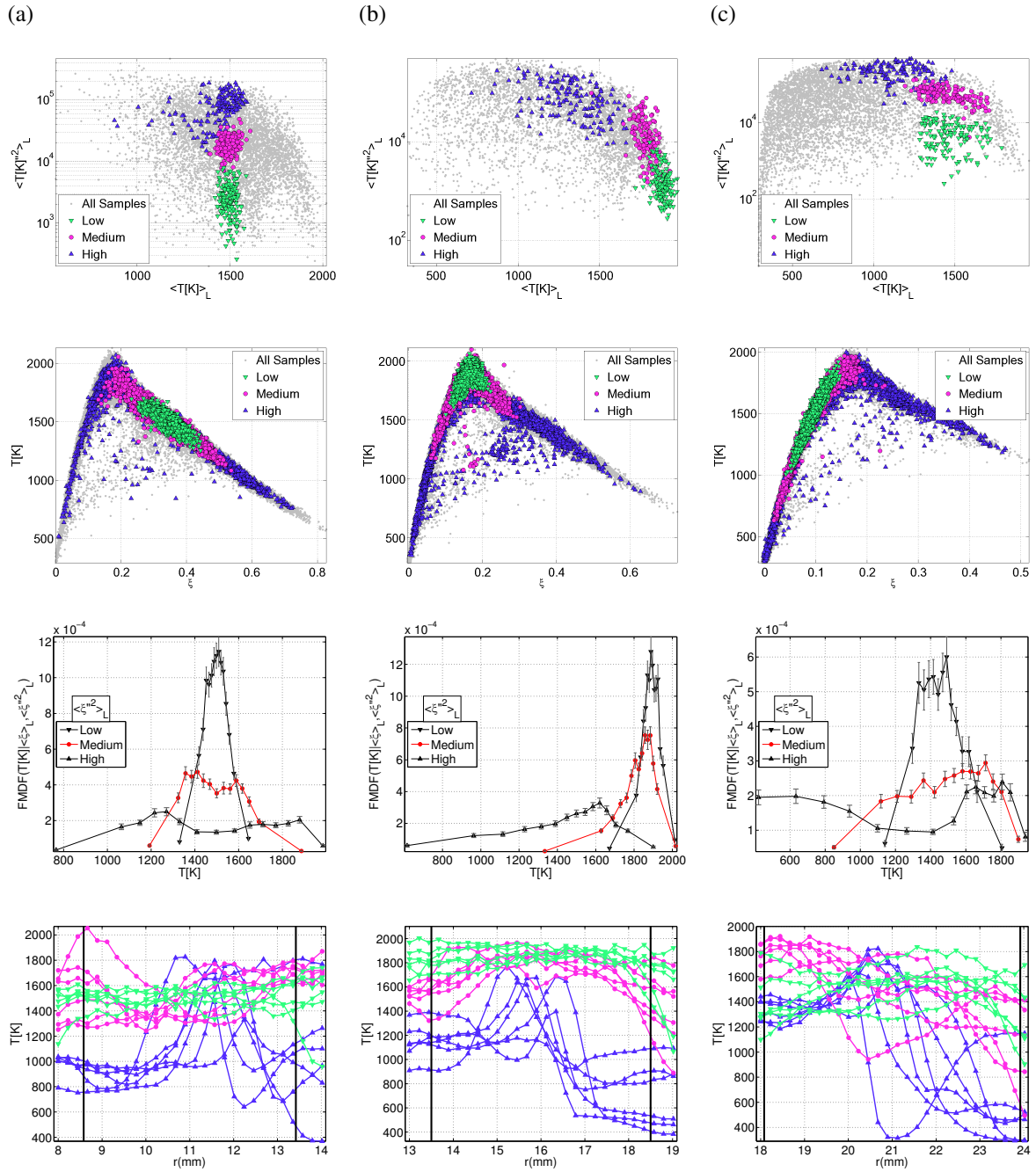

Figure 6: The FMDF conditioning bins, Temperature versus the mixture fraction data of each bin, FMDFs of the temperature, and the corresponding representative spatial temperature structures for fuel- (a) rich, (b) stoichiometric, (c) lean values of $\langle\xi\rangle_L$ and low, medium and high values of $\langle\xi''^2\rangle_L$ at $x/d = 20$ and $\Delta_L/\lambda_B = 40$ (DLR-A).

pockets of the scalar. The peaks of the FMDFs level off on the fuel-rich side because the variation in the density there is small. FMDFs conditioned on low values of the variance are unimodal.

The corresponding FMDFs of the temperature are shown in Fig. 6. Bimodal distributions occur for

fuel- lean and rich values of the mean, and high values of SGS variance. The scatter in temperature versus the mixture fraction is also shown. The most significant number of low temperature events occurs for the stoichiometric value of the mean and high values of the SGS variance. The large number of the low temperature samples manifests itself as a broad, slowly decreasing tail of the FMDF when conditioned on high values of the SGS variance.

The correlation between mixture fraction and temperature is shown on the top row of Fig. 6. There exists both a level of unique correlation and a significant level of difference and overlap. It is likely that for low values of SGS variance, conditioning on appropriate values of the mean temperature and its SGS variance could produce results qualitatively similar to those obtained by conditioning on the functions of mixture fraction alone. But, the same is unclear for the high values of the SGS variance, where there exists a significant overlap of bins of fuel- rich, stoichiometric and lean intervals. The spatial profiles of the temperature are shown in the bottom row of Fig. 6. The profiles corresponding to the high values of the SGS variance exhibit a "bell-ramp" shapes. The "bell-ramps" produce bimodal distributions of the FMDFs of the temperature only for fuel- lean or rich value of the mixture fraction mean. For the stoichiometric values of the mean the FMDFs of the temperature are unimodal with slowly decaying long temperature tails. The "bell-ramp" temperature profiles and the temperature scatter plots suggest that, for the filter sizes considered, at least 20% of the important heat releasing phenomena and majority of the extinction phonomena occur within the subgrid.

3.4 Effect of the filter size

Recent work of Wang *et al.* [22] provides estimates of the local Batchelor scales in DLR-A and DLR-B flames. This allows us to consider FMDFs corresponding to a specific ratio Δ_L/λ_B. Table 1 shows the top hat filter widths at several locations in the flames. Those correspond to the ratio of Δ_L/λ_B of 20 and 40. Using Pope's power spectrum [36] as a model with $Re_\lambda = 130$ [22], the two ratios resolve approximately 87% and 76% of the total energy in the mixture fraction, and 20% and 7% of the corresponding dissipation. Both filter size ratios place the filter cutoff in the inertial subrange of the model power spectrum. Figure 7 shows the FMDFs conditioned on the

Table 1: Filter widths used for obtaining FMDFs in different locations in the flames.

		$\Delta_L/\lambda_B = (20\ 40)\lambda_B\ [mm]$	
x/d	r/d	DLR-A	DLR-B
10	1.0	(1.84 3.68)	(1.42 2.84)
10	1.5	(2.10 4.20)	(1.72 3.44)
20	1.4	(2.42 4.84)	(1.90 3.80)
20	2.0	(2.50 5.00)	(2.12 4.24)
20	2.6	(2.92 5.84)	(2.48 4.96)

stoichiometric value of the mixture fraction mean for the two different filter size ratios. The level of bimodality at high values of SGS variance is prominent for cases with large filter widths. In the limit as the filter size decreases to zero the "cliff" structures observed at high values of the SGS variance produce nearly uniform FMDF distributions.

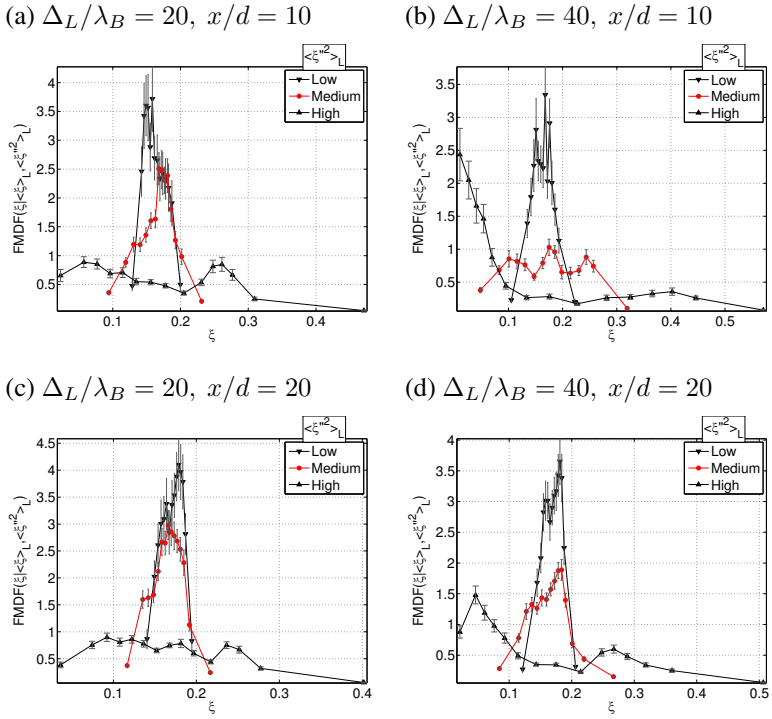

Figure 7: FMDFs of ξ for DLR-A. The conditioning $\langle\xi\rangle_L$ bin is centered at 0.167.

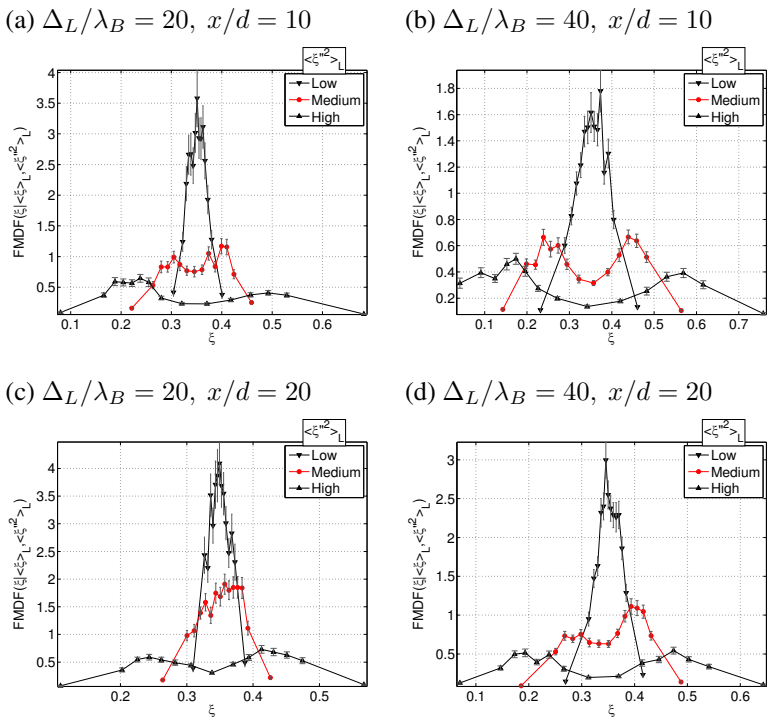

Figure 8: FMDFs of ξ for DLR-A. The conditioning $\langle\xi\rangle_L$ bin is centered at 0.35.

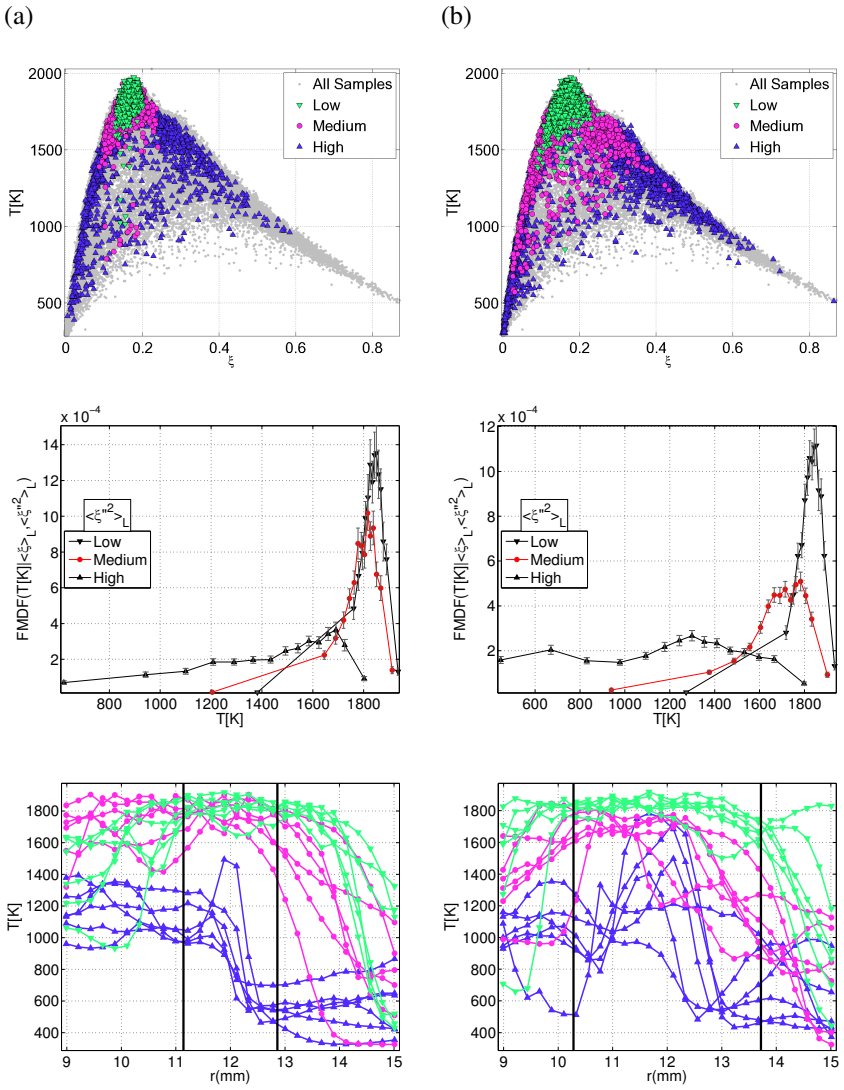

Figure 9: Temperature versus ξ data for each bin, FMDFs of temperature and the corresponding representative spatial structures for Δ_L/λ_B (a) 20, (b) 40. The conditioning $\langle\xi\rangle_L$ bin is centered at 0.167 and low, medium and high values of $\langle\xi''^2\rangle_L$ at $x/d = 10$ (DLR-B).

Figure 8 shows the FMDFs conditioned on the fuel-rich value of the mixture fraction mean for the same locations and filter size ratios as in Fig. 7. A stronger bimodal distributions persist at all locations even for medium values of the SGS variance. However, increasing of the filter size tends to accentuate the bimodality and broaden the sample space of the FMDFs. This latter effect occurs for all distributions regardless of the flame location or conditioning criteria. The temperature FMDFs for different filter size ratios are shown in Fig. 9 for DLR-B flame. The figure also shows the temperature scatter plots and the corresponding spatial temperature profiles for various conditioning bins. Similarly to the FMDFs of the mixture fraction, the increase in filter size broadens the sample space range of the FMDFs of temperature. A comparison of the scatter plots with the FMDFs reveals that the broad tails of the FMDFs are due to increasing number of low temperature events. The larger filter size increases the probability of these events to occur within

the subgrid. The probability of finding extinction events for the small filter size is approximately 20%. When the filter size is doubled the probability of finding the extinction events significantly increases, as evidenced by the increased number of extinction events for the medium value of the SGS variance. The spatial structures corresponding to the FMDFs of the temperature for the highest values of the SGS variance exhibit a"bell-ramp" profiles.

3.5 Effect of the Reynolds number

In this section we compare the effects of the Reynolds number on the FMDFs. Figure 10 shows the FMDFs conditioned on the stoichiometric value of the mean mixture fraction and low, medium and high values of the SGS variance. The FMDF profiles for both flames exhibit nearly identical features. In the near field of both flames, trimodal distributions occur for the medium value of the SGS variance. However, at downstream locations only unimodal distributions exist. All of the high values of the variance exhibit bimodal distributions. Figure 11 shows the FMDFs conditioned on

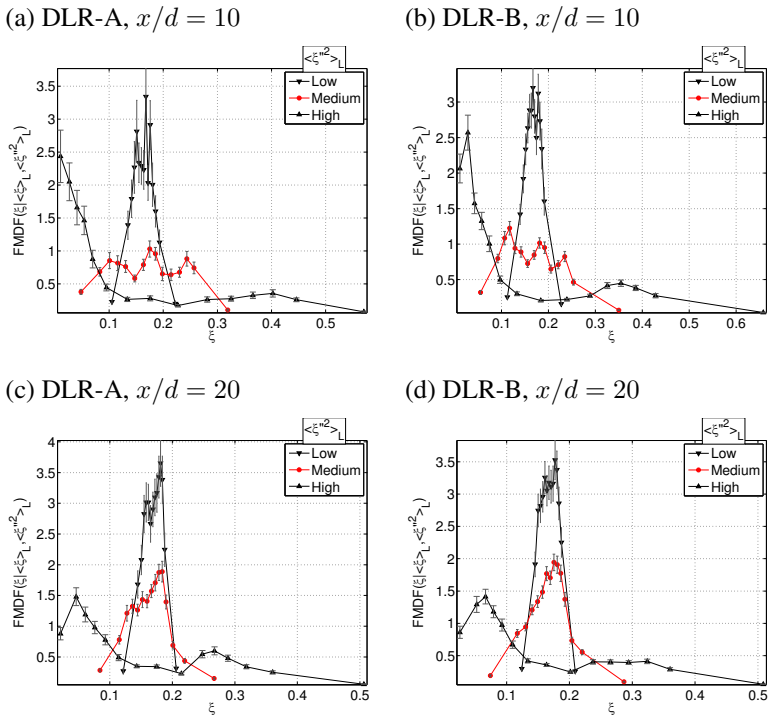

Figure 10: FMDFs of ξ for $\Delta_L/\lambda_B = 40$. The conditioning $\langle\xi\rangle_L$ bin is centered at 0.167.

the fuel-rich value of the mean mixture fraction. Similarly to the previous result, the distributions for both flames are similar. Bimodality is pronounced for all high values of the SGS variance and is seen to diminish for the medium SGS variances. The bimodality also diminishes downstream in both flames. The temperature scatter plots, FMDF distributions and the spatial temperature profiles are shown in Fig. 12 for both flames. The scatter plots indicate that the DLR-B flame has many extinct samples that contribute to the FMDF conditioned on the high SGS variance. These samples contribute to the broadening of the low temperature tail of the FMDF.

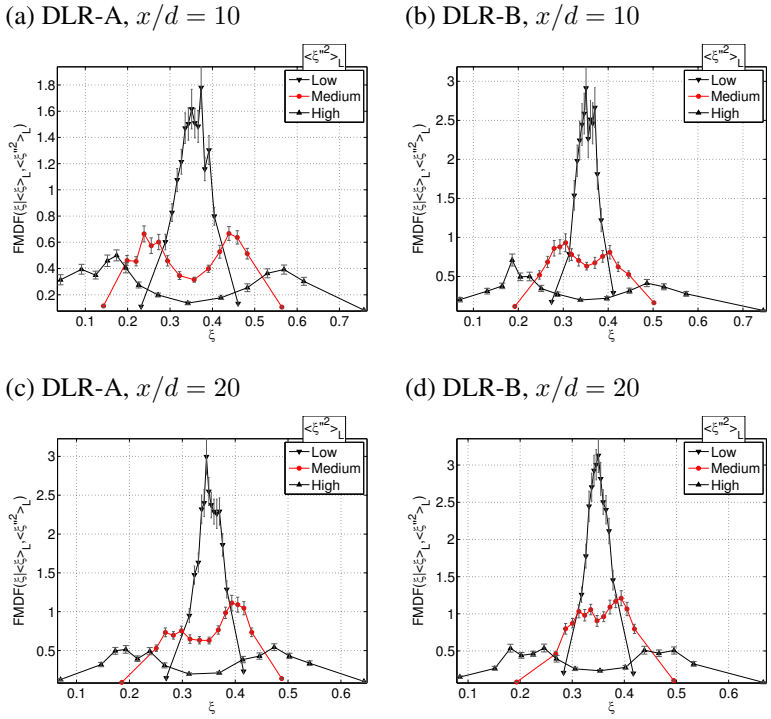

Figure 11: FMDFs of ξ for $\Delta_L/\lambda_B = 40$. The conditioning $\langle\xi\rangle_L$ bin is centered at 0.35.

4 Conclusions

FMDFs of the mixture fraction and the temperature conditioned on the Favré filtered mixture fraction and its SGS variance have been studied in DLR-A and DLR-B flames. A top hat filter was used for all cases. Two different ratios of the filter width to experimentally determined Batchelor scale were considered (20 and 40). The FMDFs were constructed by binning the mixture fraction and temperature data. The bin widths were chosen to maintain a fixed level of the statistical accuracy. The Monte-Carlo Bootstrap method was used to obtain statistical confidence intervals of the results. Results were acquired for fuel- lean, stoichiometric and rich intervals of the Favré filtered mixture fraction. Further conditioning on low, medium, or high values of the SGS variance revealed a range of distributions indicative of the level of the SGS mixing. "Cliff"-like spatial structures were found in data conditioned on several medium and all high values of the SGS mixture fraction. "Bell-ramp" structures were found in the temperature profiles under the same conditions. "Cliffs" indicate non-premixed SGS regions of the scalar and produce bimodal FMDFs of the mixture fraction. The non-premixed regions were composed of fuel- lean, stoichiometric, or rich pockets separated by a "cliff" spatial structure. Statistically significant trimodal FMDFs were also observed in both flames for the large filter widths. The trimodal FMDFs contained unmixed fuel- lean, stoichiometric and rich pockets of the mixture fraction. The FMDFs conditioned on low values of SGS variance produced a unimodal and symmetric distributions indicating a well mixed subgrid. The scatter plots of the temperature versus mixture fraction for low values of SGS variance showed all temperatures near the equilibrium conditions. The same scatter plots for high values of SGS variance contained extinction events. Results highlight the need for SGS combustion models to represent a broad range of SGS mixing phenomena that may lead to

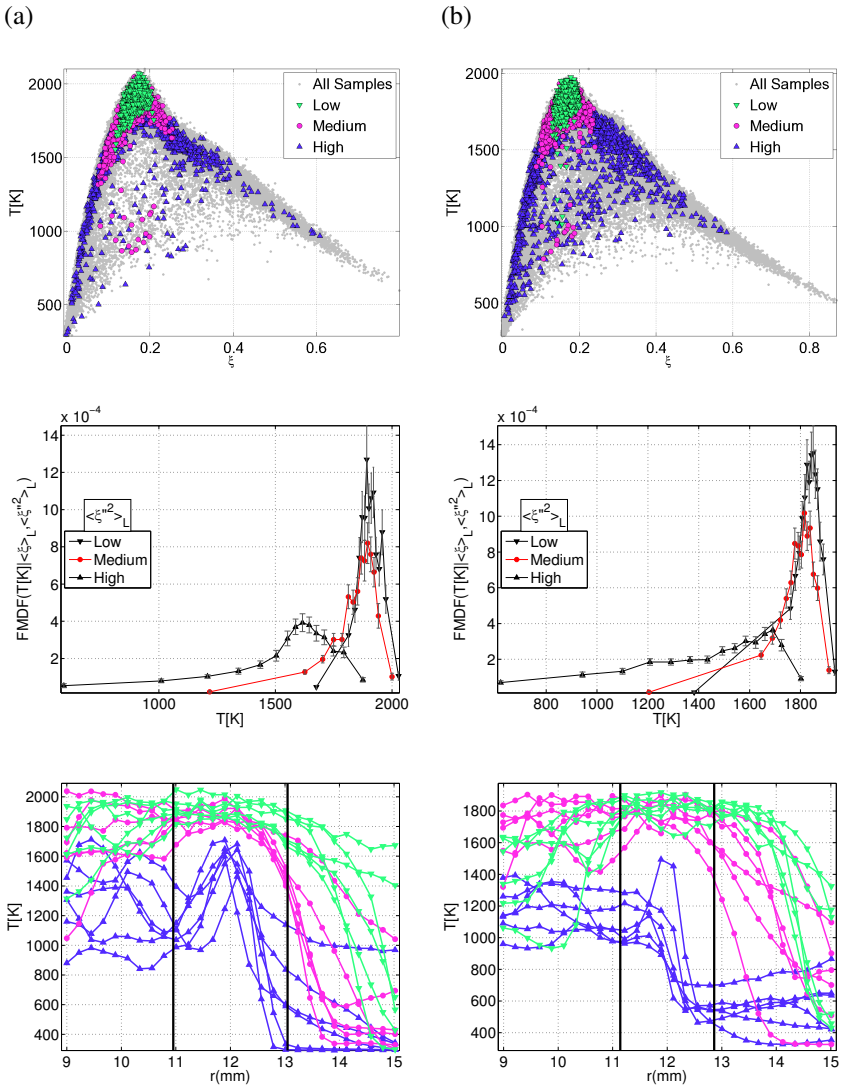

Figure 12: Temperature versus ξ data for each bin, FMDFs of temperature and the corresponding representative spatial structures for $\Delta_L/\lambda_B = 20$ and (a) DLR-A, (b) DLR-B. The conditioning $\langle\xi\rangle_L$ bin is centered at 0.167 and low, medium and high values of $\langle\xi''^2\rangle_L$ at $x/d = 10$.

near equilibrium combustion, or extinction.

Acknowledgments

I would like thank Dr. Jackson Mayo for his discussions about the Monte-Carlo Bootstrap method that proved invaluable in assessing the statistical significance of the FMDF distributions. The U. S. Department of Energy, Office of Basic Energy Sciences, Division of Chemical Sciences, Geosciences, and Biosciences supported this work. Sandia National Laboratories is a multiprogram laboratory operated by Sandia Corporation, a Lockheed Martin Company, for the United States Department of Energy under contract DE-AC04-94-AL85000.

References

[1] P. J. Colucci, F. A. Jaberi, P. Givi, and S. B. Pope. *Phys. Fluids*, 10 (1998) 499–515.

[2] F. A. Jaberi, P. J. Colucci, S. James, P. Givi, and S. B. Pope. *J. Fluid Mech.*, 401 (1999) 85–121.

[3] P. Givi. *AIAA J.*, 44 (2006) 16–23.

[4] X. Y. Zhou and J. C. F. Pereira. *Flow, Turb. Combust.*, 64 (2000) 279–300.

[5] M. R. H. Sheikhi, T. G. Drozda, P. Givi, F. A. Jaberi, and S. B. Pope. *Proc. Combust. Inst.*, 30 (2005) 549–556.

[6] V. Raman, H. Pitsch, and R. O. Fox. *Combust. Flame*, 143 (2005) 56–78.

[7] M.D. Carrara and P.E. DesJardin. *Int. J. Multiphase Flow*, 32 (2006) 365–384.

[8] S. James, J. Zhu, and M.S. Anand. *Proc. Combust. Inst.*, 31 (2007) 1737–1745.

[9] T. G. Drozda, M. R. H. Sheikhi, C. K. Madnia, and P. Givi. *Flow. Turbul. Combust.*, 78 (2007) 35–67.

[10] V. Raman and H. Pitsch. *Proc. Combust. Inst.*, 31 (2007) 1711–1719.

[11] S. S. Girimaji. *Combust. Sci. Technol.*, 78 (1991) 177–196.

[12] S. H. Frankel, V. Adumitroaie, C. K. Madnia, and P. Givi. Large eddy simulations of turbulent reacting flows by assumed PDF methods. In S. A. Ragab and U. Piomelli, editors, *Engineering Applications of Large Eddy Simulations*, pages 81–101. ASME, FED-Vol. 162, New York, NY, 1993.

[13] C. Wall, S. J. Boersma, and P. Moin. *Phys. Fluids*, 12 (2000) 2522–2529.

[14] J. P. Mellado, S. Sarkar, and C. Pantano. *Phys. Fluids*, 15 (2003) 3280–3307.

[15] R. W. Bilger. *Phys. Fluids A.*, 5 (1993) 436–444.

[16] W. K. Bushe and H. Steiner. *Phys. Fluids*, 11 (1999) 1896–1906.

[17] C. Tong. *Phys. Fluids*, 13 (2001) 2923–2937.

[18] D. Wang, C. Tong, and S. B. Pope. *Phys. Fluids*, 16 (2004) 3599–3613.

[19] D. Wang, C. Tong, R. S. Barlow, and A. N. Karpetis. *Proc. Combust. Inst.*, 31 (2007) 1533–1541.

[20] D. Wang and C. Tong. *Phys. Fluids*, 14 (2003) 2170–2185.

[21] A. G. Rajagopalan and C. Tong. *Phys. Fluids*, 15 (2003) 227–244.

[22] G. Wang, A. N. Karpetis, and R. S. Barlow. *Combust. Flame*, 148 (2007) 62–75.

[23] W. Meier, R.S. Barlow, Y.L. Chen, and J.Y. Chen. *Combustion and Flame*, 123 (2000) 326–343.

[24] Sandia National Laboratories, TNF Workshop website, DLR Flames. `http://www.ca.sandia.gov/TNF/DataArch/DLRflames.html`, 2007.

[25] A.N. Karpetis and R.S. Barlow. *Proc. Combust. Inst.*, 29 (2003) 1929–1936.

[26] R.S. Barlow and A.N. Karpetis. *Flow. Turbul. Combust.*, 72 (2004) 427–448.

[27] R.S. Barlow and A.N. Karpetis. *Proc. Combust. Inst.*, 30 (2005) 673–680.

[28] R.S. Barlow and P.C. Miles. *Proc. Combust. Inst.*, 28 (2000) 269–277.

[29] R. W. Bilger, S. H. Starner, and R. J. Kee. *Combust. Flame*, 80 (1990) 135–149.

[30] E. E. O'Brien. The probability density function (PDF) approach to reacting turbulent flows. In P. A. Libby and F. A. Williams, editors, *Turbulent Reacting Flows*, Vol. 44 of *Topics in Applied Physics*, chapter 5, pages 185–218. Springer-Verlag, Heidelberg, 1980.

[31] S. B. Pope. *Prog. Energy Combust. Sci.*, 11 (1985) 119–192.

[32] H. Pitsch. *Annu. Rev. Fluid Mech.*, 38 (2006) 453–482.

[33] R. L. Launer and G. N. Wilkinson, editors. *Robustness in Statistics*. Academic Press, New York, 1979.

[34] P. J. Huber. *Robust Statistics*. Wiley, New York, 1981.

[35] W. H. Press, B. P. Flannery, S. A. Teukolsky, and W. T. Vetterling. *Numerical Recipes in FORTRAN: The Art of Scientific Computing*. Cambridge University Press, 2 edition, Sep 1992.

[36] S. B. Pope. *Turbulent Flows*. Cambridge University Press, Cambridge, UK, 2000.